Environmental Science and Pollution Research
https://doi.org/10.1007/s11356-023-28359-2

CHALLENGES IN ENVIRONMENTAL SCIENCE & ENGINEERING: WATER SUSTAINABILITY THROUGH THE APPLICATION OF ADVANCED AND NATURE-BASED SYSTEMS

Facile synthesis of polyethyleneimine-modified cellulose nanocrystal/silica hybrid aerogel for CO_2 adsorption

Quyen Kim Thi Doan[1] · **Kung Yuh Chiang**[1]

Received: 3 March 2023 / Accepted: 16 June 2023

Abstract
Cellulose nanocrystal (CNC)/silica hybrid aerogel (CSA) was synthesized from CNC and sodium silicate hybridization using the one-step sol–gel method under atmospheric drying. At a weight ratio of CNC to silica of 1:1, the obtained CSA-1 had a highly porous network, a high specific area of 479 m^2 g^{-1}, and a CO_2 adsorption capacity of 0.25 mmol g^{-1}. Then, polyethyleneimine (PEI) was impregnated on CSA-1 to improve CO_2 adsorption performance. The parameters governing CO_2 adsorption performance on CSA-PEI, such as temperatures (70–120 °C) and PEI concentrations (40–60 wt%), were investigated systematically. The optimum adsorbent (CSA-PEI50) exhibited an excellent CO_2 adsorption capacity of 2.35 mmol g^{-1} at 70 °C and a PEI concentration of 50 wt%. The adsorption mechanism of CSA-PEI50 was elucidated by analyzing many adsorption kinetic models. The CO_2 adsorption behaviors of CSA-PEI at various temperatures and PEI concentrations had the goodness of fit with the Avrami kinetic model, which can correspond to the multiple adsorption mechanism. The Avrami model also showed fractional reaction orders in a range of 0.352–0.613, and the root mean square error is negligible. Moreover, the rate-limiting kinetic analysis showed that film diffusion and intraparticle diffusion resistance controlled the adsorption speed and dominated the subsequent adsorption stages, respectively. The CSA-PEI50 also exhibited excellent stability after ten adsorption–desorption cycles. This study illustrated that CSA-PEI was a potential adsorbent for CO_2 capture from flue gas.

Keywords Cellulose nanocrystal · Silica · Hybrid aerogel · Amine modification · CO_2 adsorption · Adsorption kinetic · One-pot synthesis

Introduction

Global warming has become more severe during this decade. Carbon dioxide (CO_2) is a primary reason for global warming and extreme weather. If CO_2 concentrations continue to rise, the earth's temperature could increase by 1.5℃ by 2050. Consequently, natural disasters have become much worse. According to the International Energy Agency, burning fossil fuels is the main cause of CO_2 emissions into the atmosphere (99% of the world's annual CO_2 emissions, which add up total about 32 Gt) (Lee and Park 2015). Thus, capturing CO_2 from these sources is essential to prevent or delay the increase in CO_2 concentration in the air.

Among the currently available CO_2 capture technologies, post-combustion capture via the adsorption process is the most widely used. The adsorption process usually uses a solid adsorbent to capture CO_2 molecules. Solid adsorbent materials have shown high CO_2 adsorption efficiency in published research, such as activated carbon (Wickramaratne and Jaroniec 2013), zeolite 13X (Chen et al. 2014), metal–organic frameworks (Gaikwad et al. 2019), composite material (Papa et al. 2019; Jeong-Potter and Farrauto 2021), bio-based aerogel (Wang and Okubayashi 2019; Mohd et al. 2021), and cellulose-based hybrid aerogel (Jiang et al. 2018; Tang et al. 2019). Among them, cellulose-based hybrid aerogel and composite materials have recently gained more attention because these materials refer to the synergistic combination of multi-scale components that can boost

Responsible Editor: Tito Roberto Cadaval Jr

✉ Kung Yuh Chiang
kychiang@ncu.edu.tw

[1] Graduate Institute of Environmental Engineering, National Central University, Zhongda Rd., Zhongli District, Taoyuan City, Taiwan

Published online: 08 July 2023

mechanical strength and chemical stability (Gu et al. 2018). The composite materials displayed prominent characteristics such as a large surface area, prolonged mechanical stability, significant adsorption capacity, high selectivity, and sensitivity (Hasan et al. 2021a, b). Therefore, composite materials are potential materials for the treatment of various pollutants, such as heavy metals (Awual et al. 2019a, b; Hasan et al. 2021a, b; Salman et al. 2021), phosphates (Awual 2019), toxic nitrite (Awual et al. 2019a, b), toxic dyes (Islam et al. 2021; Kubra et al. 2021), and CO_2 adsorption (Jeong-Potter and Farrauto 2021). However, composite materials still have limitations, such as the requirement of high temperatures during the synthesis process, high material cost, and complicated synthesis procedures (Hasan et al. 2021a, b).

Compared to composite materials, cellulose-based hybrid aerogels have a more straightforward preparation process and are more environmentally friendly due to the advantages of cellulose properties, such as low cost, sustainability, and biodegradability. Additionally, aerogel materials have a much higher porosity than composite materials. For example, the porosity of composite materials was approximately 35.1% for graphite composites (Wang et al. 2022), 57% for geopolymer-hydrotalcite composites (Papa et al. 2019), while the porosity of cellulose-based hybrid aerogel materials was around 90–99%, which was ideal for facilitating air flow and aiding in the capture process (Zheng et al. 2014; Zhou et al. 2019; Kiliyankil et al. 2021). Therefore, cellulose-based hybrid aerogel is a promising adsorbent for CO_2 adsorption.

The cellulose-based hybrid aerogel is commonly synthesized by combining the cellulose and silica (Si) components. Cellulose aerogel is low density, high porosity, and flexible but has low thermal stability. In comparison, silica aerogel is exceptionally thermally stable. Hence, the silica component is frequently utilized in producing cellulosic-based hybrid aerogel. Moreover, the cellulose nanomaterials come in a variety of hierarchical forms. Cellulose nanocrystal stands out due to their robust mechanical properties, elasticity, biocompatibility, low density, biodegradability, non-toxic component, and excellent mechanical properties (Kaur et al. 2021). Therefore, the cellulose nanocrystal is a good template for synthesizing hybrid aerogel (Jiang et al. 2018).

Cellulose/Si hybrid aerogel was prepared via a two-step gelation and impregnation method. In this procedure, cellulose component was first dissolved in solvents such as ionic liquid (1-ethyl-3-methylimidazolium acetate)—dimethyl sulfoxide (Demilecamps et al. 2015), and sodium hydroxide-thiourea (Shi et al. 2013). The dissolved cellulose was then regenerated in a non-solvent to form a cellulose hydrogel, which was then immersed in silicon alkoxides. Finally, the impregnated cellulose alcogel was obtained under supercritical or freeze drying. However, the conventional method required a lot of preparation time, and major silica sources from silicon alkoxides are toxic and expensive. Therefore, recent research has been focusing on the one-step sol–gel approach to reduce reaction time and synthesis costs, along with the use of sodium silicate solution as a low-cost and non-hazardous source of silica. For instance, Miao et al. developed a cellulose/Si hybrid aerogel by mixing sodium silicate and cellulose using the one-step sol–gel method. The prepared hybrid aerogel displayed high CO_2 adsorption efficiency and selectivity (Miao et al. 2020a, b). Zhou et al. also synthesized a cellulose whisker/Si hybrid aerogel using the one-step sol–gel method. The synthesized hybrid aerogel possessed a multiple function, in which silica content can enhance thermal stability, and cellulose whiskers work as the structural skeleton to strengthen the mechanical properties and improves CO_2 capture performance (Zhou et al. 2021).

However, the cellulose/silica hybrid aerogel material has not yet been commercialized. One limitation is the drying process. Drying is an essential step in the formation of the porous structure. The technologies commonly used include freeze-drying and supercritical drying, which can remove the hydrogel liquid phase while maintaining a highly porous solid structure. However, this drying method uses special equipment with extreme drying conditions, consuming great amounts of energy. Therefore, developing aerogel materials under atmospheric drying conditions could be a viable method to commercialize aerogel materials for CO_2 adsorption. However, there are few studies on preparing cellulose/silica hybrid aerogel materials under normal drying conditions because this method creates a capillary pressure that collapses the material pore structure. More researches are needed to develop hybrid aerogel materials with improved characteristics under air drying (Li et al. 2019).

Furthermore, improving CO_2 adsorption performance is also essential for developing a new adsorbent. Amine-modified cellulose/Si aerogel is a priority strategy to enhance the CO_2 capture capacity. There are various amine types that can modify the hybrid aerogel surface. There are two amine kinds, including amine group I and amine group II. Amine group I is loaded onto the adsorbent surface by impregnation through physical binding. In contrast, amine group II will form a covalent bond with the adsorbent (Keshavarz et al. 2021). The impregnation method is commonly used for the preparation of amine-embedded porous materials due to its simplicity and low cost. Linear tetraethylenepentamine (TEPA) and branched polyethyleneimines (PEI) are frequently utilized for physical impregnation because of their high amine content and inexpensive cost. However, using branched PEI with a high percentage of tertiary amines has the significant practical benefit of requiring less energy for CO_2 desorption than primary or secondary amines in TEPA (Choi et al. 2021). However, the surface modification of cellulose nanocrystal/silica hybrid aerogels with PEI and the

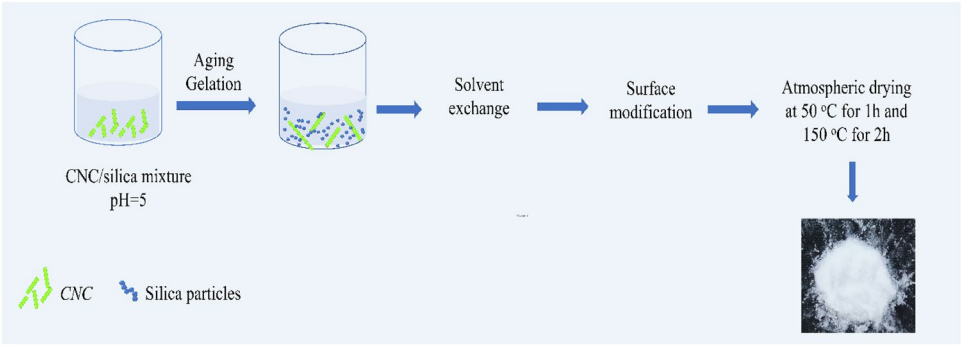

Scheme 1 A schematic description of CSA preparation

kinetic analysis of CO_2 adsorption on this material have yet to be extensively studied. The adsorption kinetic analysis is useful for providing insight about the adsorption rate and adsorption mechanism for the solid adsorbent. Serna-Guerrero and Sayari (2010) investigated kinetic models to predict the CO_2 molecule adsorption mechanism onto PEI-impregnated mesoporous silica under various adsorption temperatures. They indicated that multiple adsorption pathways controlled the entire adsorption process (Serna-Guerrero and Sayari 2010). Wang and Okubayashi (2019) applied different adsorption kinetic models to analyze the CO_2 adsorption behavior of PEI-cross-linked cellulose aerogel, indicating that the chemical adsorption governed the CO_2 adsorption process (Wang and Okubayashi 2019). These studies contributed helpful knowledge of the adsorption mechanism and provided a practical method for forecasting the adsorbent and adsorbate adsorption behavior. Therefore, investigating the adsorption kinetics is vital to elucidate the CO_2 adsorption mechanism of PEI-modified cellulose nanocrystal/silica hybrid aerogel.

This study synthesizes and characterizes the cellulose nanocrystal (CNC)/Si hybrid aerogel properties using the one-step sol–gel preparation method along with atmospheric drying. The obtained hybrid aerogel was modified with PEI to investigate the amine modification effect on CO_2 adsorption capacity and kinetics. The PEI-modified CNC/Si hybrid aerogel adsorption behavior and diffusion mechanism were analyzed using pseudo-first-order, pseudo-second-order, Avrami fractional-order models, and rate-limiting kinetic models.

Materials and methods

Materials

Microcrystalline cellulose (MCC) was prepared from cotton cloth waste in our previous study using hydrochloric hydrolysis acid (Doan and Chiang 2022), sodium silicate solution with density of 1.39 g mL^{-1}, composition of sodium oxide of 10.6% and silicon dioxide of 26.5% (Sigma-Aldrich), sulfuric acid (H_2SO_4, 96%) (Aencore company-Australia), hydrochloric acid (HCl, 37%) (Fisher chemical-Canada), trimethylchlorosilane (TMCS, 98%) (Themo scientific), branched polyethyleneimine (PEI, $M_w = 800$) (Sigma-Aldrich), hexane (99%) (Sigma-Aldrich), and methanol (99.9%) (Sigma-Aldrich).

Cellulose nanocrystal preparation

CNC was prepared from MCC using H_2SO_4 acid hydrolysis. The MCC was added into 61 wt.% sulfuric acid at a ratio of MCC to acid solution of 1:30 mg L^{-1}. The mixture was heated for 55 min at 50 °C in a water bath circulator. After hydrolysis, the solution was cooled by adding pure water and centrifuged at 5000 rpm until the supernatant became turbid. The obtained precipitate underwent dialysis using dialysis tubing cellulose membrane (molecular weight cutoff of 12–14 kDa) against pure water to remove the residual acid. The dialysis process was completed when the filtrate achieved a neutral pH. The obtained CNC was then homogenized using an ultrasonic bath for 15 min. The CNC suspension was dried at − 80℃ for 24 h using a freeze-dryer (Model FDU-2110, Tokyo Rikakikai Co., Ltd).

CNC/silica aerogel preparation

CSA aerogel was synthesized using one-pot synthesis, as shown in Scheme 1. The sodium silica solution was diluted to a specific gravity of 1.05. Different amounts of CNC suspension at 8 wt.% were added to a given amount of sodium silica solution and vigorously stirred for 2 h under room temperature. The CNC/silica (CNC/Si) mixture was then sonicated for 2 min (sonics Vibra cell, VCX750, 20% Ampl) to form a homogeneous mixture. The weight ratio of CNC suspension to silica was investigated, including 0:1, 1:1, 1.5:1, and 2:1. Afterward, the mixture was hydrolyzed using 1N HCl with an adjusted pH of 5.5. The hydrolyzed CNC/Si mixture was poured into cylindrical molds for gelation at room temperature. After gelation, CNC/silica gels strengthened network integrity by aging for 3 h at 50℃. The gels were then immersed in pure water and kept for 24 h at

50℃. The pure water was replaced each 4 h. The CNC/Si hydrogels were exchanged with methanol for 24 h at 40℃. Furthermore, the CNC/Si gel surface was modified for 20 h at room temperature using a TMCS/n-hexane solution. The molar ratio of TMCS/n-hexane and silica was 1:7 and 4:1, respectively. CSA-(*x*), where *x* represents the weight ratio of CNC to silica, was obtained by atmospheric drying at 50℃ for 1 h and 120℃ for 2 h.

PEI-modified CSA material preparation

PEI was used to modify the CSA-1 surface using the impregnation method. PEI was added into methanol and stirred for 20 min until completely dissolved. A given amount of CSA-1 was then added to the mixture and stirred for 2 h at room temperature. The slurry was dried in a vacuum oven at 80 °C for 24 h after being modified. The obtained materials were named CSA-PEI-*y*, where *y* represents the theoretical PEI load weight in the final material. The theoretical PEI load weight ranged from 40 to 60%.

Characterization of CSA and CSA-PEI materials

Dynamic rheological analysis

The dynamic rheological characteristics of CNC/silica gel were determined at 25℃ using an MCR 302 Rheometer. The measuring equipment configuration included a parallel plate measuring plate (PP25) with an angular frequency range of 0.1 to 100 rad/s. Each sample was measured two times.

Morphological structure

The CSA and CSA-PEI surface morphology was visualized using scanning electron microscopy (SEM) (SU-8200, Hitachi). The equipment was operated at 10 kV accelerating voltage and 7.9 mm working distance. High-resolution transmission electron microscopy (HR-TEM) was operated at 80 kV accelerating voltage for determining the morphology of CNC and CSA-1 samples. The elemental composition of the CSA-1 surface was analyzed via energy dispersive X-ray spectroscopy (EDX).

Pore structure analysis

The sample specific area and pore characteristics were measured at 77 K using a nitrogen adsorption–desorption isotherm (Autosorb iQ equipment, Anton Paar). The sample was first degassed at 100℃ for 24 h to remove moisture and volatile components. The Brunauer–Emmett–Teller (BET) method was used to determine the specific area in the relative P/Po pressure range of 0.05–0.3. The Barrett Joyner Halenda (BJH) model was employed to calculate pore size distribution. The total pore volume was calculated based on the amount of adsorbed N_2 at a P/Po pressure ratio of 0.98.

Thermal analysis

The sample thermal properties were analyzed via a thermogravimetric analyzer (TGA) (STA 7300, High-Tech Science Corporation) under 100 mL min^{-1} nitrogen gas and a heating rate of 10℃ min^{-1}. The sample weight of 5–6 g was loaded into a ceramic pan. Each sample was tested twice.

Functional groups analysis

Attenuated total reflectance—Fourier transform infrared spectrometer (ATR-FTIR) from PerkinElmer Frontier spectrometer ((PerkinElmer, Inc.) was used to determine the CSA-PE150 functional groups. The spectra were collected at room temperature with a wavenumber range of 4000 to 650 cm^{-1} and a spectra resolution of 4 cm^{-1}.

CO_2 adsorption

The CSA and CSA-PEI sample CO_2 adsorption tests were implemented using the TGA. This method was also used in literature reviews (Jiang et al. 2018; Wang and Okubayashi 2019). About 5 g of the sample was loaded into a platinum sample pan. Before the adsorption test, the sample was heated to 100℃ for 60 min under atmospheric pressure and 100 mL min^{-1} nitrogen to remove any moisture and impurities content that the sample may have adsorbed from the air. The CO_2 adsorption process was carried out by switching the gas flow to pure dry CO_2 (100 mL/min, 1 atm) until no further weight increase was observed. CO_2 uptake analysis was implemented at different CNC to silica (0:1, 1:1, 1.5:1, and 2:1) blending ratios, temperatures (30, 50, 70, 90, and 120℃), and PEI contents (40, 50, and 60 wt.%). The CO_2 adsorption capacity was determined via the weight change of the adsorbent during CO_2 measurement (Wang and Okubayashi 2019).

For the CO_2 desorption process, the nitrogen gas flow was switched, and the adsorption temperature was heated to 105℃ for 60 min. The CO_2 adsorption regeneration capacity was investigated on the CSA-PEI50 under pure dry CO_2 at 70℃ with ten cycles of CO_2 adsorption–desorption measurement. Amine efficiency was calculated from the CO_2 adsorption capacity and nitrogen (N) content. The N content was determined using a Vario Micro cube CHONS elemental analyzer (Elemental Analysensysteme GmbH, Germany). The amine efficiency equation is shown in Eq. (1) (Bai et al. 2019):

$$\text{Amine efficiency} = \frac{\text{CO}_2\text{adsorption capacity}}{\text{N content}} \quad (1)$$

CO_2 adsorption kinetic

Adsorption kinetics can provide valuable information on the adsorption rate, establishing the time needed for the adsorption process to reach equilibrium (Keshavarz et al. 2021). Kinetic models can explain details about the adsorption pathways and potential underlying mechanisms. Many kinetic models are applied to explain the adsorption process characteristics. The pseudo-first-order, pseudo-second-order, Avrami, Boyd's film-diffusion, and intraparticle diffusion kinetic models were applied in this study to describe the dynamic adsorption process. Root mean square error (RMSE) (Eq. (2)) is used to assess the model regression precision. The different kinetic equations are shown in Table 1 as follows.

$$\text{RMSE} = \sqrt{\frac{\sum_1^N \left(q_{exp} - q_{cal}\right)^2}{N}} \times 100\% \quad (2)$$

where q_{exp} and q_{cal} are the CO_2 adsorption capacity of the observed and predicted values using kinetic models, respectively (mmol g^{-1}), and N is the number of observations.

Results and discussions

CNC/Si gel, CSA, and CSA-PEI50 sample characterizations

Rheological property of CNC/Si gel

The CNC amount influence on the mechanical properties of the CNC/Si gel structure was investigated using rheological analysis. Figure 1a shows that the CNC/silica was successfully formed during the aging process. Figure 1b displays that the storage modulus (G') was higher than the loss modulus (G") in all samples, indicating that the samples possessed a solid-like structure.

As shown in Fig. 1b, the G' of CNC/silica gel increased substantially when the blending amount of CNC was increased from CNC/Si-0 to CNC/Si-1, meaning that the CNC component played a significant role in strengthening the CNC/Si gel structure. CNC contributed to the strong primary skeleton in the gel network. At the same time, the condensed colloidal silica works as a bridge to interconnect the CNC with the gel matrix (Jiang et al. 2018). However, as the amount of CNC components increased, the G' of CNC/Si-1.5 and CNC/Si-2 decreased gradually, indicating that adding too many CNC components can disrupt the matrix structure and reduce the gel structure mechanical strength. Based on the analysis of gel strength, it can be identified

Table 1 Kinetic models for CO_2 adsorption process

Model	Expression	Parameters	Ref
Pseudo-first-order kinetic model	$q_t = q_e[1 - \exp(-k_1 t)]$ (3)	q_t: adsorption amount at a given time (t), mmol g^{-1} q_e: adsorption amount at equilibrium, mmol g^{-1} k_1: first order kinetic constant, min^{-1}	(Wang and Okubayashi 2019)
Pseudo-second-order kinetic model	$q_t = \frac{q_e^2 k_2 t}{1 + q_e k_2 t}$ (4)	k_2: second order kinetic constant, mmol g^{-1} min^{-1}	(Wang and Okubayashi 2019)
Avrami kinetic model	$q_t = q_e[1 - \exp(-(k_A t)^{n_A})]$ (5)	k_A: Avrami rate constant, min^{-1} n_A: the exponents in the Avrami fractional kinetic model	(Serna-Guerrero and Sayari 2010)
Boyd's film-diffusion	$B_t = -ln\frac{\pi^2}{6} - \ln(1 - F)$ for $F > 0.85$ (6)	$F = q_t/q_e$: the fractional adsorption capacity B_t: Boyd number	(Song et al. 2016)
Interparticle diffusion model	$B_t = (\sqrt{\pi} - \sqrt{\pi - \frac{\pi^2 F}{3}})^2$ for $F \le 0.85$ (7) $1 - \frac{q_t}{q_e} \approx \frac{6}{\pi^2}\exp\left(-\frac{\pi^2 D_c t}{r_p^2}\right)$ (8)	Assuming that the majority of particle shapes are spheres and $F \ge 0.7$ D_c: is the effective intraparticle diffusion coefficient r_p: radius dimension of particle	(Song et al. 2016)
Intraparticle diffusion	$q_t = k_{id} t^{0.5} + C$ (9)	k_{id}: intraparticle kinetic constant mmol g^{-1} $min^{-0.5}$ C: a constant related to the thickness of the boundary layer	(Wang and Okubayashi 2019)

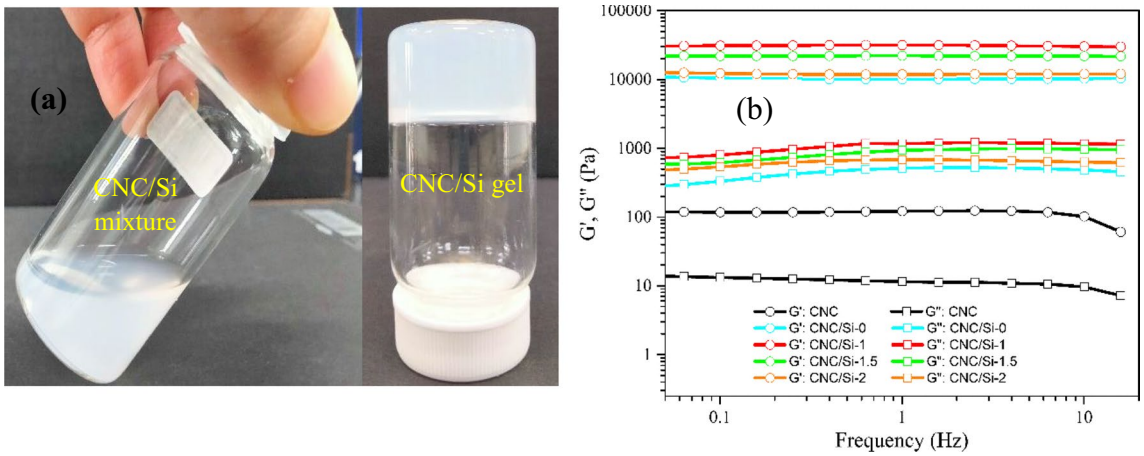

Fig. 1 Photographs of CNC/Si mixture and CNC/Si gel after aging process (**a**), G' and G" of CNC and CNC/Si gel under various blending ratio between CNC and sodium silicate

that the weight ratio of CNC to Si of 1:1 (CNC/Si-1) is an optimum concentration for enhancing the skeleton structure in hybrid aerogel materials.

Morphological structure of CSA and CSA-PEI50 samples

SEM results for CSA and CSA-PEI50 are presented in Fig. 2. As shown in Fig. 2a, the CSA-0 possessed a porous three-dimensional structure under atmospheric drying. This finding indicated that the solvent exchange and surface modification overcame the capillary tension and produced a hydrophobic aerogel surface (Khedkar et al. 2019). The hydrophobic property of the CSA sample provides a stable structure against humidity when dried under ambient pressure. Moreover, the CSA structure from CSA-1 to CSA-2 remained a porous network as the CNC content increased. It was not easy to recognize the CNC component in Fig. 2 because the CNC is enclosed in aerogel and embedded deep within the CSA structure (Zhou et al. 2021).

These CSA samples contained secondary silica particles that were larger and more evident than CSA-0. These findings can be explained by the rod-shaped CNC (Fig. S1) providing a strong framework for the silica particles to easily attach, resulting in the robust silica aerogel skeleton. The elemental composition analysis of CSA-1 (Fig. S2) using energy dispersive X-ray illustrates that the carbon (C), oxygen (O), and silicon (Si) components were dominant in the sample. On the other hand, the amounts of chloride (Cl) and sodium (Na) were negligible and not detected. These findings indicated that the impure components of Cl and Na were removed entirely during the CSA preparation process. From Fig. 2e, after modifying CSA-1 with 50 wt.% PEI, the CSA-PEI50 surface was entirely flat. Its pore structure was filled by PEI molecules, causing the adsorbent to lose its porous feature (Zhou et al. 2021).

Thermostability analysis

The thermostability properties of CNC, CSA, and CSA-PEI are shown in Fig. 3. For CSA samples, CSA-0 presented an insignificant weight loss about 9% at 800℃. The CSA-0 main degradation temperature occurred at 500–600℃, with a minor weight loss assigned to methyl groups degradation from TMCS surface modification. This result indicated that silica aerogel possessed high thermal stability (Jiang et al. 2018). The thermal behavior was changed when CNC was added to the silica aerogel matrix. CSA-1, CSA-1.5, and CSA-2 samples showed peak degradation in the 325 to 340℃ range, corresponding to the decomposition of cellulose. The sample weight loss increased as the blending ratio between CNC and Si increased from 1 to 2.

Although the CSA sample thermal stability minorly reduced with the increase in CNC amount, the thermal behavior of these materials improved significantly compared to the original CNC materials. This result indicated that CNC penetrates the silica matrix and binds tightly to the silica particles (Zhou et al. 2021). After modification, the thermal properties of CSA-PEI were divided into three stages. The first stage was below 180 °C. The sample mass degraded considerably at a temperature around 55℃ due to water evaporation and adsorbed gas in the air by adsorbent materials. As the temperature was raised to 110℃, the CSA-PEI weight loss corresponded to the evaporation of absorbed water or low molecular impurities (Mazrouaa et al. 2019).

The second stage was in the 200 to 430℃ range, which is the main degradation of CSA-PEI samples. The weight loss came mainly from the PEI and CNC component decomposition. The CSA-PEI sample weight loss increased from 40.30

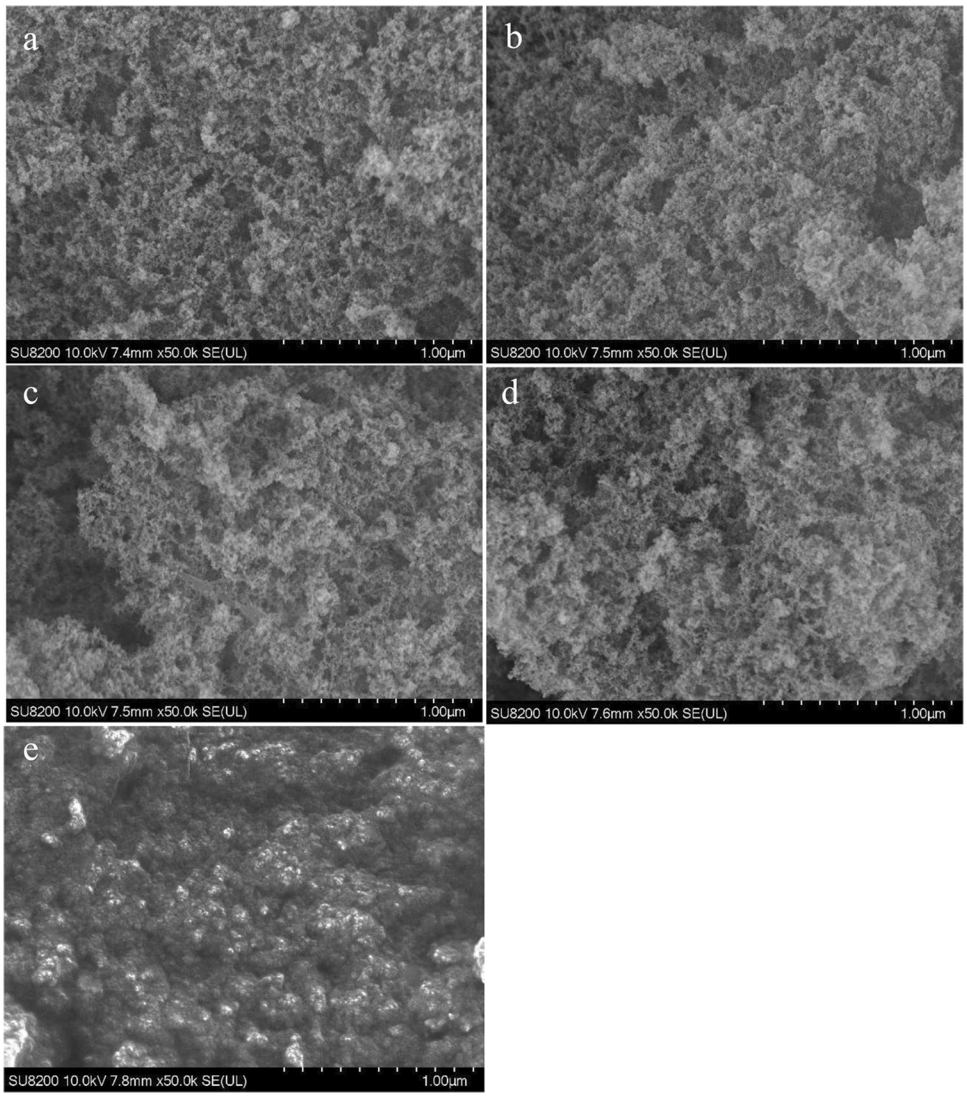

Fig. 2 SEM images of CSA-0 (**a**), CSA-1 (**b**), CSA-1.5 (**c**), CSA-2 (**d**), and CSA-PEI50 (**e**)

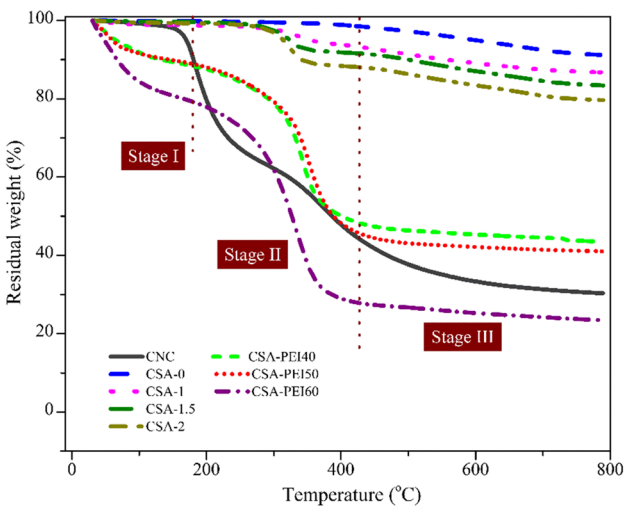

Fig. 3 CNC, CSA, and CSA-PEI sample thermal properties

to 44.21% when the PEI concentration was loaded into the CSA-1 sample increased from 40 to 60 wt.%, respectively. The final stage ranged from 430 to 800℃, and the modified sample weight gradually decreased. Furthermore, the more PEI concentration was modified on the CSA surface, the less residual weight it had. These findings indicated that the thermal stability of the PEI content was weak and easy to decompose at high temperatures (Li et al. 2017).

Pore structure analysis

The nitrogen adsorption–desorption isotherms and pore size distribution of CSA samples and CSA-PEI40 are displayed in Fig. 4. As shown in Fig. 4a, all CSA curves correspond to IV isotherms with a type H3 hysteresis loop, which correlated to mesopores and the slit-shape pores (Li et al. 2017). The pore size distribution curves of all CSA samples exhibited one dominant peak (Fig. 4c).

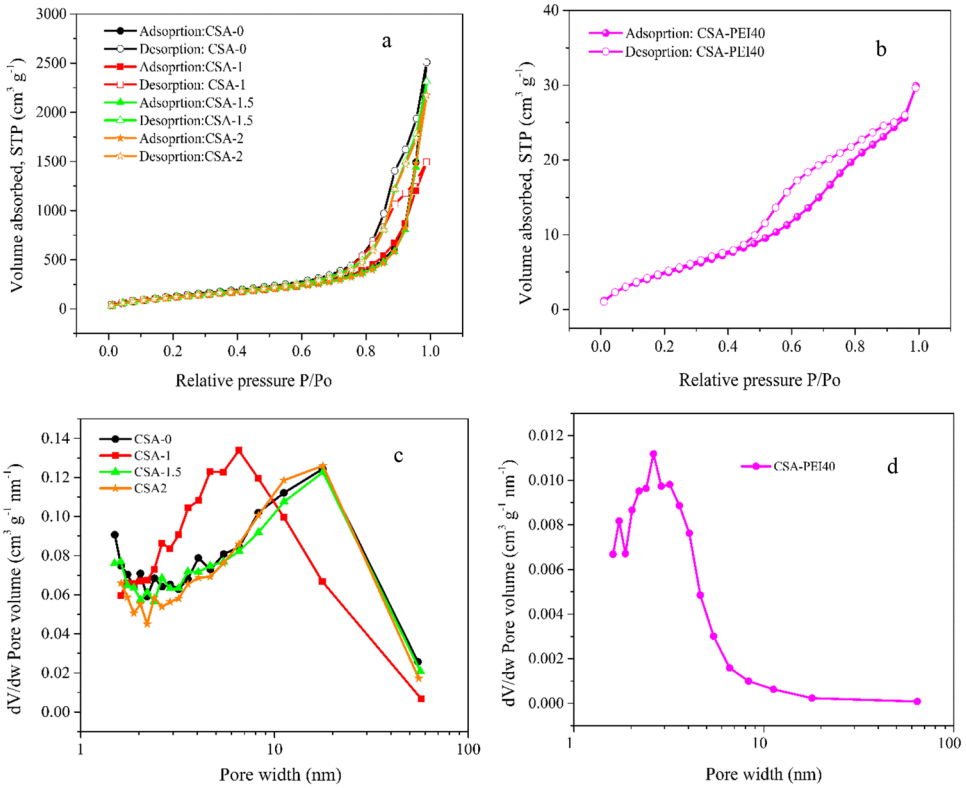

Fig. 4 N_2 adsorption–desorption curve of CSA samples (**a**) and CSA-PEI40 (**b**). Pore size distribution of CSA samples (**c**) and CSA-PEI40 (**d**)

Table 2 Textural properties and nitrogen (N) content of CSA and CSA-PEI samples

Sample	BET surface area ($m^2\ g^{-1}$)	Pore volume ($cm^3\ g^{-1}$)	Average pore size (nm)	N content (wt.%)
CSA-0	540.28	3.88	14.3	n.d
CSA-1	479.08	2.31	9.64	n.d
CSA-1.5	501.79	3.58	14.25	n.d
CSA-2	483.16	3.36	13.91	n.d
CSA-PEI40	20.96	0.05	4.42	11.71
CSA-PEI50	n.a	n.a	n.a	14.76
CSA-PEI60	n.a	n.a	n.a	15.14

n.a, not available; *n.d*, not detected

The peak position of the CSA-1 sample is distinct from other CSA samples. The curve for CSA-1 displayed a maximum pore size of 6.5 nm, while the different samples had the same peak positions with a maximum pore size of 20 nm. The specific surface area (S_{BET}) of CSA samples (Table 2) indicated that the CNC-added samples decreased the S_{BET} and pore volume. This can be explained by CNC taking up much space and the cross-linking between CNC and secondary silica particles blocking the pore interior (Li et al. 2017).

The isotherm analysis of PEI-modified CSA material is also investigated and presented in Fig. 4b. CSA-PEI40 illustrated the type IV isotherm with an H2-type hysteresis, corresponding to a mesoporous material (Salman et al. 2023a, b). However, the volume absorbed by CSA-PEI40 was much lower than that of CSA samples. The type H2 hysteresis loop also demonstrated the multifaceted pore structure with typical ink bottle-shaped pores (Zhou et al. 2021). Previous studies have shown that the ink bottle-shaped pore structure had a higher adsorption capacity than the slit-shaped pore structure (Liu et al. 2020). Therefore, transforming the pore structure from slit-shaped to ink bottle-shaped after modification with PEI may positively enhance the CO_2 adsorption capacity of the CSA-PEI materials. However, modification with PEI significantly reduces the specific surface area of the CSA-PEI40 material. This is because the PEI component could fill the pores of CSA material (Bai et al. 2019). The phenomenon was similar to reducing the specific area in composite adsorbents preparation (Hasan et al. 2023; Salman et al. 2023a, b). In addition, the pore structure surface gradually becomes rougher and denser because PEI can occupy the pores (Sanz et al. 2010). Besides, amination on CSA material was confirmed using nitrogen (N) content analysis. As shown in Table 2, N content increased when the PEI concentration increased. A higher N content could establish more covalent bonds with CO_2, anticipating greater CO_2 adsorption capacity.

CO_2 adsorption performance

CNC to silica ratio effect

The CSA sample CO_2 adsorption capability with varying proportions of CNC to silica is depicted in Fig. 5. The increase in CNC ratio from CSA-0 to CSA-1 resulted in an increase in the CO_2 system capacity. However, once the CNC quantity was increased even further, a tendency toward decreased adsorption capability was seen. The maximum CO_2 capacity was found in CSA-1, which measured 0.25 mmol/g. The CSA samples had a high surface area and pore volume, which facilitated CO_2 capture and may be associated with physical adsorption (Miao et al. 2020a, b). Moreover, the CSA-1 three-dimensional network structure was more robust and stable than the other materials; the CO_2 molecules quickly entered the material network and increased the adsorption capacity (Kiliyankil et al. 2021). In addition, CSA-1 was selected for PEI modification because of its high adsorption capacity and stable material properties.

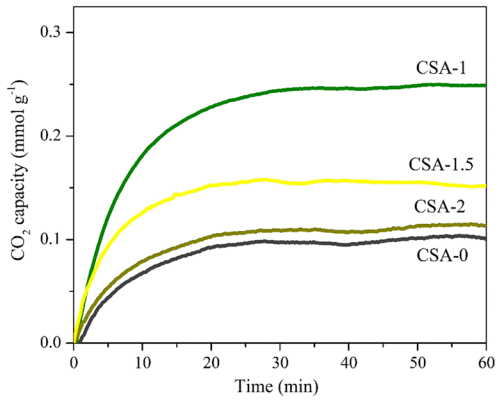

Fig. 5 CSA-x sample CO_2 adsorption capacity at room temperature and atmospheric pressure

The CO_2 adsorption kinetics and adsorption mechanisms of CSA-PEI were further investigated in the following.

Temperature adsorption and PEI content effects

The CO_2 adsorption capacity on CSA-PEI samples was investigated under adsorption conditions, including different adsorption temperatures and PEI concentrations (Fig. 6). Figure 6a shows the CO_2 adsorption capacity on CSA-PEI50 under different adsorption temperatures from 30 to 120℃. The CO_2 adsorption at equilibrium increased from 0.9 to 2.61 mmol g^{-1} when the temperature increased from 30 to 90℃, respectively. This phenomenon was similar to the CO_2 capture study using PEI-impregnation resin adsorbent (Bai et al. 2019). It was observed that the CO_2 capture performance of CSA-PEI50 samples was substantially enhanced compared with CSA-1 material. This is because the CSA-PEI50 material can adsorb CO_2 through physical interactions and chemical interactions between amino groups on CSA-PEI50 and CO_2 molecules (Lee and Park 2015). The reaction was illustrated as follows:

$$CO_2 + 2RNH_2 \rightarrow RNHCOO^- + RNH_3^+ \quad (10)$$

$$CO_2 + 2R_2NH \rightarrow R_2NCOO^- + R_2NH_2^+ \quad (11)$$

FTIR spectra were also examined to confirm that the amino groups successfully interacted with CO_2 molecules, as shown in Fig. S3. The wavenumber at 1550 cm^{-1} was considered to be (N)COO-asymmetric stretching (Sepahvand et al. 2020), corresponding to the formation of ammonium carbamates. Moreover, the temperature increase can lead to an increase in the CO_2 molecule diffusion rate, which can easily access the amine groups on CSA-PEI50. However, The adsorption capacity displayed a declining trend when the adsorption temperature increased to 120 °C due to the naturally CO_2 adsorption exothermic process (Bai et al. 2019). The CSA-PEI50 displayed a high adsorption capacity in the temperature range

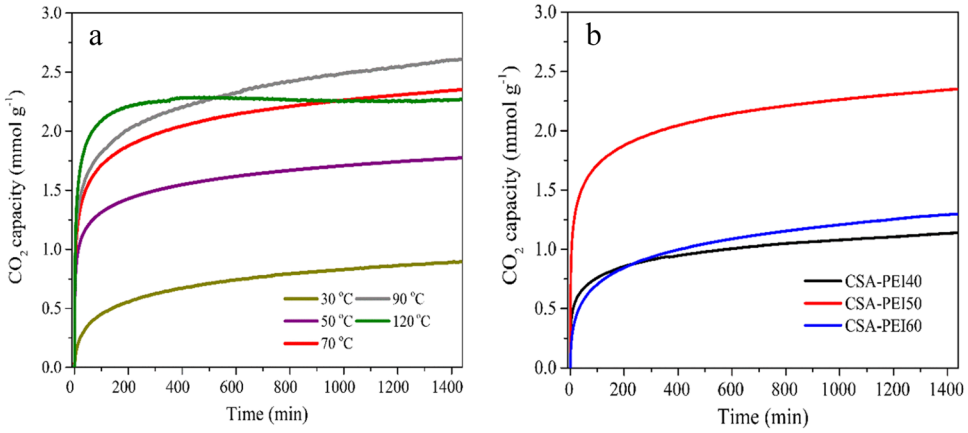

Fig. 6 CSA-PEI50 CO_2 adsorption capacity under various adsorption temperature (**a**), CSA-and PEI50 sample CO_2 adsorption capacity under different PEI contents at 70℃ (**b**)

of 70–90℃, suggesting a prospective adsorbent for CO_2 capture from flue gas. Moreover, when the adsorption temperature was increased from 50 to 70℃, the CO_2 adsorption capacity increased by 34%. In contrast, the efficiency of CO_2 adsorption only increased by 11% when the temperature was raised from 70 to 90℃. Although the maximum adsorption capacity was achieved at 90℃, the adsorption efficiency increase was not impressive. It is essential to consider both the adsorbent material's cost-effective energy consumption and durability when selecting the optimal adsorption temperature. Therefore, this study identified the optimal adsorption temperature at 70℃ for CO_2 capture.

Figure 6b shows the effect of PEI concentrations on CO_2 adsorption capacity at 70℃. The CO_2 adsorption capacity dramatically rose when the PEI concentrations were increased from 40 to 50 wt.%. The findings can be associated with increasing N content when the PEI concentration increases (as shown in Table 2). It can be confirmed that a higher N content can facilitate the creation of more covalent bonds with CO_2, resulting in an increased capacity for CO_2 adsorption (Wang and Okubayashi 2019). However, the CO_2 adsorption capacity exhibited a decreasing trend when the PEI content was increased to 60 wt.%. This is because the PEI-loaded material pore volume can be blocked with a further increase in PEI concentration, hindering the intraparticle diffusion of CO_2 molecules and reducing the access between CO_2 and the inner amino groups (Song et al. 2016). Therefore, the PEI concentration of 50 wt% was suitable for impregnation and improving the CO_2 adsorption capacity. Therefore, the PEI concentration of 50 wt% was suitable for impregnation and improving the CO_2 adsorption capacity.

Furthermore, the CO_2 adsorption performance also exhibited by parameter of amine efficiency. The mentioned equation illustrated a maximum theoretical amine efficiency of 0.5 mmol CO_2 per mmol N under anhydrous conditions (Sanz et al. 2010). Besides, CSA-PEI50 had the highest amine efficiency of 0.24 mmol CO_2/mmol N at 90 °C (Table 3). The result cannot achieve its theoretical value as expected because not all amino functional groups can react with CO_2 in practice. The branched PEI contains about 25% of tertiary amines, which cannot react with CO_2 under anhydrous conditions (Sanz et al. 2010).

In addition, the CSA-PEI50 displayed a higher CO_2 adsorption performance than previous studies in Table 4. Besides, the CSA-PEI50 was easily prepared and produced by a low material cost. In contrast, almost all the cited research used silicon alkoxides as the silica source, which are too expensive and toxic. These aerogel materials were made using a complicated synthesis process along with supercritical or freeze-drying, which consumes more energy and is not feasible for practical applications. Therefore, the CSA-PEI50 in this study may be considered as a cost-effective material and is a potential adsorbent for CO_2 adsorption in scale-up studies.

Table 3 CO_2 adsorption capacity and amine efficiency of CSA-PEI samples

Sample	Adsorption temperature (°C)	CO_2 adsorption capacity (mmol g^{-1})	Amine efficiency (mmol CO_2/mmol N)
CSA-PEI40	70	1.15	0.14
CSA-PEI50	30	0.90	0.09
CSA-PEI50	50	1.76	0.15
CSA-PEI50	70	2.36	0.22
CSA-PEI50	90	2.61	0.24
CSA-PEI50	120	2.27	0.22
CSA-PEI60	70	1.30	0.12

CO_2 adsorption kinetic

Apparent kinetic analysis

Figure 7 shows the CO_2 adsorption kinetics of CSA-PEI50 at different adsorption temperatures. At all temperature ranges, the pseudo-first-order and pseudo-second-order models fitted well with the experimental data within the initial 5 min. After this time, these models underestimated the equilibrium amount of CO_2 adsorbed. A previous study indicated that the CO_2 adsorption process followed pseudo-first-order model, which corresponds to the physical adsorption. The pseudo-second-order model relates to the rate-determining step and is considered a chemical reaction between CO_2 molecules and the adsorbent (Song et al. 2016). However, the CO_2 adsorption over the amine-modified adsorbent can involve both physical and chemical adsorption (Yang et al. 2022). Hence, it is challenging to predict the CO_2 molecule adsorption mechanism on CSA-PEI using the pseudo-first-order and pseudo-second-order kinetic models. The Avrami model provided a good fit for the experimental CO_2 uptake during the whole adsorption process with low percent standard deviation values (Table 5).

As shown in Table 5, the RSME of the Avrami model was much smaller than that of the pseudo-first-order and pseudo-second-order models, which was consistent with the relevant data presented in Fig. 7. The CO_2 adsorption process can be accurately described by the Avrami model, which represents complex CO_2 adsorption pathways (Guo et al. 2019). This result was in line with the reported study, which the authors mentioned that the CO_2 adsorption kinetic of the composite aerogel material was well predicted via the Avrami model (Zhou et al. 2021). Furthermore, when the temperature was raised from 30 to 70℃, the kinetic rate constant of the Avrami model increased. The kinetic rate constant remained stable at 90℃ with a further temperature increase. However, when the temperature was elevated to 120℃, the kinetic rate constant increased significantly. The

Table 4 CSA-PEI50 CO_2 adsorption capacities' comparison with various aerogel types

Aerogel	Precursor	Drying method	Amine type, modification method	T (°C)	P (bar)	Ads. Capacity (mmol g^{-1})	Ref
CSA-PEI50	CNC, sodium silicate solution	Atmospheric drying	50 wt.% PEI (M_w = 800), impregnation	70	1	2.36	This study
Amine-silica aerogel	TEOs	Supercritical drying	2.17 mmol g^{-1} APTES, chemical grafting	50	1	1.19	(Cui et al. 2011)
Amine-silica aerogel	MTES/ MTMS	Supercritical conditions	Amino-alkytrialkoxysilane	40	1	1.81	(Begag et al. 2013)
Amine-silica aerogel	TMOS	Supercritical drying	Tri-APTMS, physical impregnation	22	1	0.87	(Wörmeyer and Smirnova 2013)
Commercial Silica aerogel	n.a	n.a	Tri-APTMS, chemical grafting	25	1	1.64	(Linneen et al. 2014)
Amine-silica aerogel	TEOS	Supercritical drying	APTES, chemical grafting	50	1	3.04	(Kong et al. 2016a, b)
Amine-cellulose aerogel	Cellulose triacetate	Supercritical drying	PEI, chemical grafting	40	1	2.31	(Wang and Okubayashi 2019)
Amine-nanocellulose aerogel	Microcrystalline cellulose	Freeze drying	AEAPMDS, chemical grafting	25	1	1.59	(Zhang et al. 2020)
Amine-nanocrystalline cellulose	Oil palm empty fruit bunch fiber	Freeze drying	APTMS, chemical grafting	25	1	0.20	(Mohd et al. 2021)
Amine hybrid zirconia/silica aerogel	Zirconium(IV) n-propoxide	Supercritical drying	APTES, chemical grafting	70	1	2.00	(Kong et al. 2016a, b)
Amine-modified cellulose nanofibril/ silica hybrid aerogel	Cellulose nanofibril, sodium silicate	Freeze drying	30 wt.% APTES, chemical grafting	25	1	1.49	(Jiang et al. 2018)

APTES, (3-aminopropyl) triethoxysilane; *APTMS*, 3-trimethoxysilylpropyl) diethylenetriamine; *AEAPMDS*, (2-aminoethyl) (3-amino-propyl) methyldimethoxyansile; *MTES*, methyltriethoxysilane; *MTMS*, methyltrimethoxysilane; *TEOS*, tetraethyl orthosilicate; *n.a*, not available

findings indicated that the high temperature had a significant effect on the CO_2 transfer rate into adsorbents. However, the desorption process can coincide when the temperature is raised too high, decreasing CO_2 adsorption capacity. The adsorption temperature at 70 °C was therefore an excellent choice for the CSA-PEI50 material.

The Avarmi model was also applied to investigate the PEI content effect on CO_2 adsorption kinetic at 70 °C (Fig. 7f). From Table 5, the Avrami kinetic constant dramatically increased and then decreased with increasing PEI content. These findings indicated that increasing the PEI content can increase the CO_2 molecule accessibility to active amine sites. However, when the PEI concentration increased to 60 wt.%, the kinetic constant decreased significantly because the pore volume was blocked, hindering CO_2 diffusion into the amino group positions.

Diffusional mass transfer analysis

The kinetic analysis results indicated that the CO_2 adsorption process occurred through multiple pathways. Therefore, the rate-limiting models were investigated to elucidate the CO_2 adsorption mechanism. The CO_2 molecule adsorption mechanism into a porous adsorbent is as follows: (i) bulk diffusion, where the CO_2 molecules are moved from the bulk gas phase into the outer gas film around the porous adsorbent material; (ii) film diffusion, where the CO_2 molecules diffuse across the gas film; (iii) interparticle diffusion, where the CO_2 molecules diffuse into the inter-particle space; (iv) surface diffusion, where the CO_2 molecules interact with the surface sites; and (v) intraparticle diffusion, where the CO_2 molecules diffuse from the gas film into the internal surface of the adsorbent (Yoro et al. 2020). According to previous research, the bulk and surface diffusion steps are relatively rapid. Their resistance level in the adsorption process is assumed to be inconsequential (Song et al. 2016). Therefore, the current study focused only on the film, interparticle, and intraparticle diffusion models for CO_2 adsorption onto CSA-PEI materials.

Film diffusion is the most crucial stage in any adsorption process because it governs the diffusion of gases into most adsorbents (Yoro et al. 2020). Boyd's film diffusion plots under different adsorption temperatures and PEI contents are shown in Fig. 8. If the B_t plot versus t is a straight line

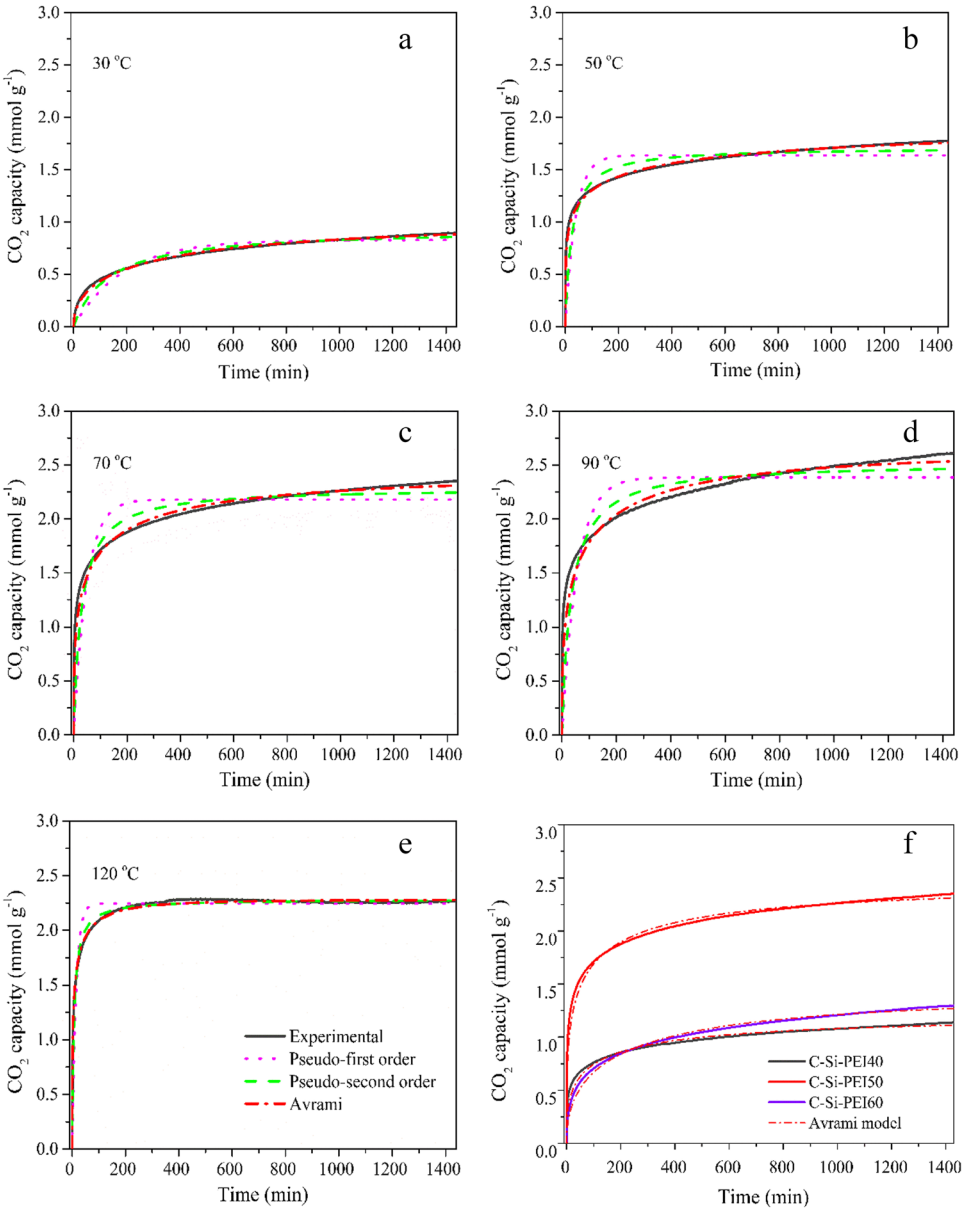

Fig. 7 Kinetic fitting using pseudo-first-order, pseudo-second-order, and Avrami model for CO_2 adsorption on CSA-PEI50 and CSA-PEI-y samples under different adsorption temperature (**a**–**e**) and different PEI contents (**f**), respectively

Table 5 CSA-PEI sample kinetic parameters under different adsorption kinetic models

Adsorption condition	Adsorption capacity (mmol g^{-1})	Pseudo-first order model			Pseudo-second order model			Avrami model			
		k_1 (min^{-1})	q_e (mmol g^{-1})	RMSE	k_2 (min^{-1})	q_e (mmol g^{-1})	RMSE	k_A (min^{-1})	q_e (mmol g^{-1})	n_A	RMSE
CSA-PEI50, 30 °C	0.90	0.005	0.83	0.057	0.008	0.84	0.033	0.004	0.87	0.613	0.009
CSA-PEI50, 50 °C	1.76	0.016	1.63	0.127	0.017	1.67	0.081	0.012	1.72	0..360	0.014
CSA-PEI50, 70 °C	2.35	0.021	2.18	0.167	0.015	2.24	0.104	0.017	2.29	0.352	0.037
CSA-PEI50, 90 °C	2.61	0.0178	2.39	0.201	0.012	2.45	0.129	0.014	2.53	0.356	0.063
CSA-PEI50, 120 °C	2.27	0.068	2.25	0.070	0.063	2.270	0.030	0.112	2.27	0.377	0.024
CSA-PEI40, 70 °C	1.15	n.a	n.a	n.a	n.a	n.a	n.a	0.001	1.11	0.390	0.022
CSA-PEI60, 70 °C	1.30	n.a	n.a	n.a	n.a	n.a	n.a	0.004	1.27	0.480	0.021

n.a, not available

through the origin, it indicates that only pore diffusion controls the adsorption process (Yoro et al. 2020). However, if the plot is non-linear or linear and does not pass through the origin, the adsorption process can be controlled by film diffusion (Song et al. 2016). As shown in Fig. 8a, b, the Boyd plots illustrate a non-linear trend, indicating that the CO_2 adsorption onto CSA-PEI samples is governed by film diffusion.

The interparticle diffusion curves under various adsorption temperatures and PEI contents are shown in Fig. 8c, d. Based on Eq. (8), a plot of ln (1-qt/qe) against time is assumed to be a linear function with an intercept with an intercept that should be equal to ln ($6/\pi^2$). However, Fig. 8c, d, displays that the plots of ln (1-qt/qe) against time were non-linear, and the intercept of these plots is not similar to ln ($6/\pi^2$) (as shown in Table 6). These findings indicated violations when assuming the interparticle diffusion model governed the rate-limiting step in CO_2 adsorption onto CSA-PEI materials under different adsorption conditions. Consequently, we can assume that there must be another rate-limiting step regulating the CO_2 adsorption onto the CSA-PEI materials (Song et al. 2016).

The intraparticle diffusion was examined for the CO_2 adsorption rate-limiting process analysis. Figures 8e and 8f illustrate the intraparticle diffusion model via the q_t versus square root (sqrt) time plot. The curves obtained under different adsorption temperatures and PEI contents showed multi-linearity. Each linear slope correlates to a natural rate-limiting step. The lowest sloping linear plot can account for the intraparticle diffusion barrier (Song et al. 2016). These findings confirmed that the CO_2 adsorption mechanism was governed by different rate-limiting steps.

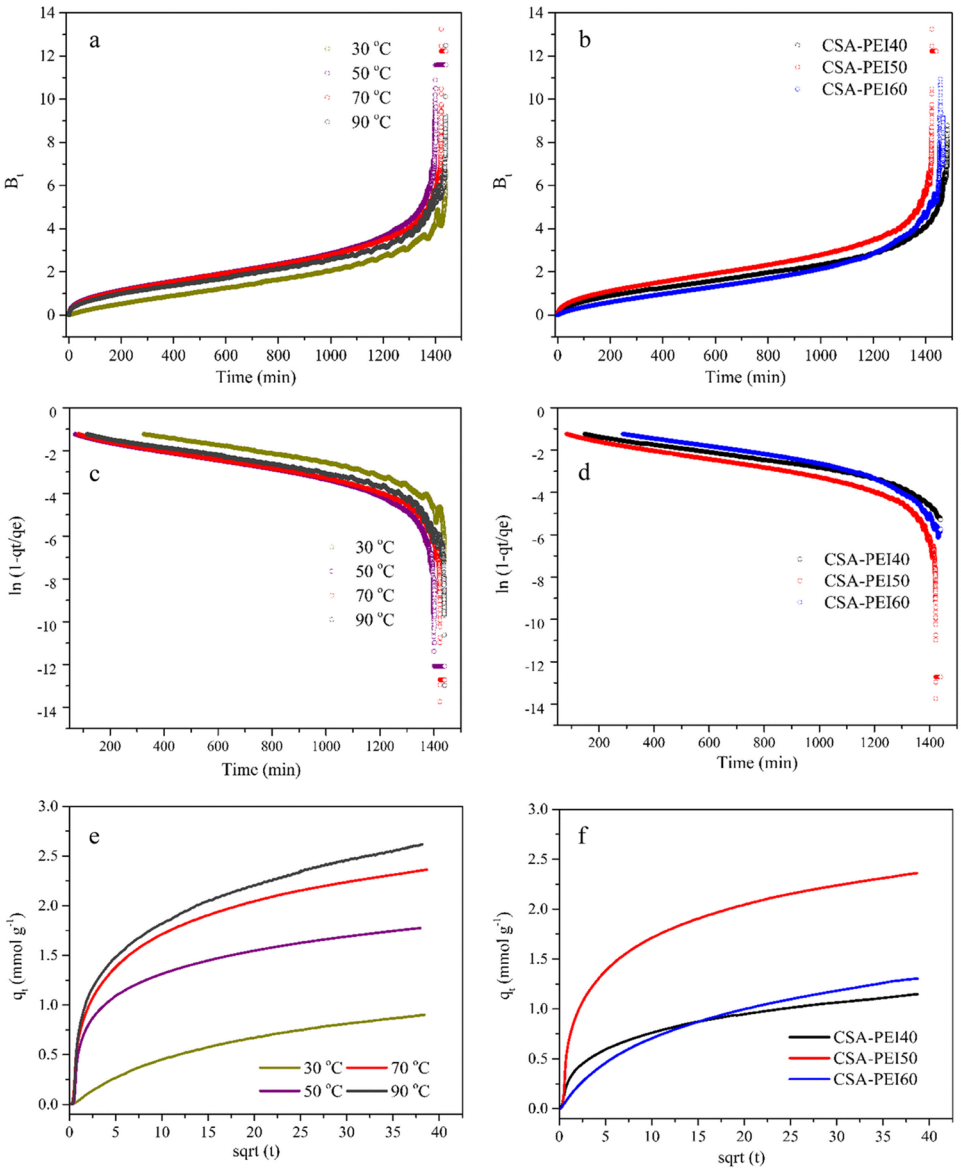

Fig. 8 Boyd's film model plots, interparticle diffusion and intraparticle diffusion for CO_2 adsorption on CSA-PEI50 under different adsorption temperatures (**a**, **c**, **e**), and on CSA-PEI samples under different PEI contents (**b**, **d**, **f**)

Table 6 Interparticle and intraparticle diffusion model parameters for CSA-PEI under various adsorption temperatures and PEI contents

Samples	Interparticle diffusion			Intraparticle diffusion		
	Slope	Intercept	R^2	K_{id} (mmol g^{-1} $min^{-0.5}$)	C	R^2
CSA-PEI50, 30 °C	−0.003	−0.023	0.899	0.012	0.454	0.994
CSA-PEI50, 50 °C	−0.004	−0.390	0.535	0.012	1.321	0.995
CSA-PEI50, 70 °C	−0.003	−0.585	0.628	0.016	1.748	0.995
CSA-PEI50, 90 °C	−0.003	−0.620	0.823	0.022	1.777	0.914
CSA-PEI40, 70 °C	−0.002	−0.750	0.931	0.010	0.758	0.996
CSA-PEI60, 70 °C	−0.003	−0.021	0.878	0.016	0.687	0.997

As a result, a CO_2 mechanism was proposed in that the CO_2 molecules initially diffused into the CSA-PEI material outer surface. The adsorption rate in this stage is controlled by film diffusion. After passing through the gas film, the CO_2 molecules diffused into the CSA-PEI pore network under intraparticle diffusion control and reacted with amino groups. As shown in Fig. 6b, the adsorption process occurs rapidly in the first 15–20 min. At this time, CO_2 molecules transferred into the pore and reacted with the inner amino groups, accelerating the CO_2 adsorption capacity. However, the CO_2 adsorption rate slowed until an equilibrium value was reached. This phenomenon may be related to the CSA-PEI material blocked pore size, which caused a significant diffusion barrier and inhibited CO_2 diffusion into the pores to react with amino groups. Therefore, it is proven that the change in CO_2 adsorption rate is greatly impacted by the CO_2 diffusion process into the pores under intraparticle diffusion.

The diffusion kinetic parameters under different adsorption conditions are presented in Table 6. The diffusion rate constant increased as the adsorption temperature increased because the CO_2 molecules tended to be more active at a higher temperature. Consequently, the CO_2 diffusion capability into the inner pore surface is enhanced. In contrast to previous reports, which found that the diffusion rate constant decreased with increasing temperature (Song et al. 2016), it is confirmed that CO_2 adsorption onto CSA-PEI materials occurs mainly at active sites inside the pore surface. This phenomenon is also contributed to by the change in the PEI physical state from increasing temperature, in which the PEI agglomeration becomes loose and the CO_2 molecules easily diffuse through the PEI phase.

CO_2 adsorption–desorption cycles

The CO_2 adsorption–desorption cycle performed on the hybrid aerogel material is an essential criterion for evaluating the feasibility of a hybrid aerogel-based adsorbent. Figure 9 displays the CO_2 capture regeneration on CSA-PEI50 with ten cycles (15,000 min) under atmospheric pressure and temperature conditions at 70℃ for adsorption and 105℃ for desorption processes. The CO_2 adsorption capacity slightly decreased after three cycles and became stable with subsequent runs that maintained 83% of the initial value. The reduction of CO_2 adsorption effectiveness can cause by a part of the pore structure collapsing and the loss of amino groups during regeneration runs. A previous study also observed a similar phenomenon (Wang and Okubayashi 2019).

Cyclic stability indicates that CSA-PEI50 is a promising material for CO_2 adsorption from flue gas. In addition, the CO_2 amount can be removed entirely from CSA-PEI50 during desorption, preventing energy penalties. It can be confirmed that lower energy consumption also leads to lower operation costs and enhances adsorption performance. Moreover, the cost of the adsorption process is substantially influenced by the choice of feedstock sources and the method used to prepare the aerogel. The qualitative comparison of energy and feedstock costs for the synthesis of aerogel materials for the CO_2 adsorption process is presented in Table 7. The CSA-PEI50 was prepared using low material costs and consumed less energy. Therefore, the CSA-PEI50 can supply a cost-effective material for CO_2

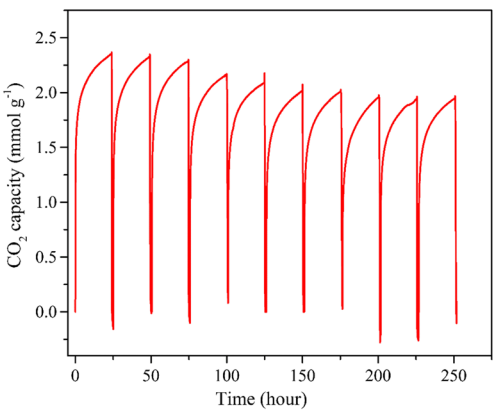

Fig. 9 Adsorption–desorption curves of CO_2 on CSA-PEI50

Table 7 Comparison of energy consumption and precursor costs of various aerogel materials for CO_2 adsorption process

Aerogel	Precursor	Amine modification	Drying method	CO_2 adsorption capacity (mmol g^{-1})	Stability performance	Energy cost of drying process	Feed stock cost	Hazard rating of precursor *	Ref
CSA-PEI50	Cotton cloth waste sodium silicate solution,	PEI, branched	Atmospheric drying	2.35	Negligible losses after 10 cycles	+	+	Moderate toxicity	This study
Composite aerogel	Cellulose, konjac glucomannan Metal organic framework (HKUST-1),	n.a	Freeze drying	3.50	Stable after 7 cycles	+ + +	+ + +	High toxicity	(Sun et al. 2022)
Amine grafted cellulose aerogel	Cellulose powder	APTES	Supercritical drying	1.20	n.a	+ +	+	Non-toxicity	(Jiang et al. 2021)
Aminosilanes grafted nanocrystalline cellulose	Oil palm empty fruit bunch	APTMS	Freeze drying	0.20	n.a	+ + +	+	Non-toxicity	(Mohd et al. 2021)
PEI-crosslinked cellulose aerogel	Cellulose	PEI, branched	Supercritical drying	2.31	Stable after 10 cycles	+ +	+	Non-toxicity	(Wang and Okubayashi 2019)
Chitosan grafted graphene oxide aerogel	Chitosan, natural graphite	n.a	Freeze drying	0.258	n.a	+ + +	+ +	Non-toxicity	(Hsan et al. 2019)
Cellulose nanofibril – silica aerogel	Rice straw, sodium silicate solution	APTES	Freeze drying	1.49	n.a	+ + +	+	Moderate toxicity	(Jiang et al. 2018)
Amine hybrid silsesquioxane aerogel	TEOS	APTES	Supercritical drying	3.04	Stable after 30 cycles	+ +	+ +	Moderate toxicity	(Kong et al. 2016a, b)
Sodium-based aerogel	Sodium carbonate, TEOs	APTES	Supercritical drying	2.51	Stable after 10 cycles	+ +	+ +	Moderate toxicity	(Yu et al. 2016)
Amine hybrid aerogel	Resorcinol, formaldehyde	APTES	Supercritical drying	1.80	Stable after 11 cycles	+ +	+ +	High toxicity	(Kong et al. 2015)
Amino functionalized silica aerogels	TMOS	APTMS	Supercritical drying	1.55	Negligible losses after 8 cycles	+ +	+ + +	High toxicity	(Wörmeyer and Smirnova 2013)

+ + +, high cost; + +, medium cost; +, low cost; *n.a*, not available; *TMOS*, tetramethyl orthosilicate; *PEI*, polyethylenimine; *APTMS*, aminosilanes (3-aminopropyl) trimethoxysilane; *APTES*, 3-aminopropyltriethoxysilane; *TEOS*, tetraethoxysilane

*The hazard rating was evaluated based on the United Nations' Globally Harmonised System of Classification and Labelling of Chemicals (GHS). The toxicity of the mixture precursor was assessed using the component with the highest toxicity level

adsorption and generate an economic incentive to proceed with scale-up studies.

Conclusions

A hybrid aerogel was successfully synthesized from the hybridization of CNC and sodium silica by a facile strategy using a one-pot sol–gel method along with atmospheric drying. The textural analysis indicated that all CNC-Si aerogel (CSA) samples illustrated a three-dimensional structure and possessed a nanoscale pore with a high specific surface area. The CSA-1 material showed the highest CO_2 adsorption capacity at 0.25 mmol/g at 30℃, 1 atm. The adsorption capacity of CSA-1 was improved by PEI modification. The effect of adsorption temperatures, PEI concentrations, and the adsorption behavior of CSA-PEI materials was investigated. The experimental CO_2 adsorption capacity of CSA-PEI50 under different temperatures (30–120℃) and PEI concentrations (40–50 wt%) was highly consistent with the Avrami kinetic model, which has been related to multiple adsorption pathways. The kinetic rate constant and CO_2 adsorption capacity increased significantly as the temperature rose from 30 to 70℃. Therefore, the adsorption temperature of 70℃ is a suitable choice for the CO_2 adsorption process, with a CO_2 adsorption capacity of 2.36 mmol g^{-1} and a kinetic rate constant of 0.017. The rate-limiting kinetic model was analyzed to elucidate the CO_2 adsorption mechanism. The CO_2 adsorption mechanism of CSA-PEI50 was governed by film diffusion and intraparticle diffusion resistances. This study aligns with previous research showing the effectiveness of amine-modified aerogel materials for CO_2 adsorption. However, the study's unique contribution is successfully synthesizing of a hybrid aerogel with improved inherent properties by incorporating CNC and Si and elucidating the adsorption mechanism by analyzing the kinetic models. CSA-PEI50 demonstrated excellent recyclability after ten adsorption–desorption cycles, indicating that it is a promising sorbent for CO_2 capture from flue gas. Moreover, the factors controlling the CO_2 adsorption process on CSA-PEI50 material, such as pressure, humidity, flow rate, and CO_2 concentration, need further research for practical implementation.

Acronyms CNC: Cellulose nanocrystal; CSA: Cellulose nanocrystal/silica hybrid aerogel; PEI: Polyethyleneimine; SEM: Scanning electron microscopy; HR-TEM: High-resolution transmission electron microscopy; EDX: Energy dispersive X-ray spectroscopy; TGA: Thermogravimetric analyzer; BET: Brunauer-Emmett-Teller; BJH: Barrett Joyner Halenda; ATR-FTIR: Attenuated total reflectance—Fourier transform infrared spectrometer; RMSE: Root mean square error

Supplementary Information The online version contains supplementary material available at https://doi.org/10.1007/s11356-023-28359-2.

Acknowledgements The author is very thankful to the Taiwan Ministry of Science and Technology (MOST) for its financial support and the Center for Advanced Instrumentation, National Central University, Taiwan, for providing analytical facilities to execute this study.

Author contribution Quyen Kim Thi Doan: conceptualization; writing—original draft; writing—review and editing. Kung-Yuh Chiang: reviewing; revising; supervising. All authors are read and approved the final manuscript.

Funding This work was supported by the Taiwan Ministry of Science and Technology (MOST) (Grand number: MOST-109–2221-E-008–023-MY2).

Data Availability The datasets obtained and analyzed during this work have been mentioned in the submitted article and supplementary materials.

Declarations

Ethical approval Not applicable.

Consent to participate Not applicable.

Consent for publication Not applicable.

Competing interests The authors declare no competing interests.

References

Awual MR (2019) Efficient phosphate removal from water for controlling eutrophication using novel composite adsorbent. J Clean Prod 228:1311–1319

Awual MR, Hasan MM, Islam A, Rahman MM, Asiri AM, Khaleque MA, Sheikh MC (2019a) Introducing an amine functionalized novel conjugate material for toxic nitrite detection and adsorption from wastewater. J Clean Prod 228:778–785

Awual MR, Hasan MM, Rahman MM, Asiri AM (2019b) Novel composite material for selective copper (II) detection and removal from aqueous media. J Mol Liq 283:772–780

Bai G, Han Y, Du P, Fei Z, Chen X, Zhang Z, Tang J, Cui M, Liu Q, Qiao X (2019) Polyethylenimine (PEI)-impregnated resin adsorbent with high efficiency and capacity for CO_2 capture from flue gas. New J Chem 43:18345–18354

Begag R, Krutka H, Dong W, Mihalcik D, Rhine W, Gould G, Baldic J, Nahass P (2013) Superhydrophobic amine functionalized aerogels as sorbents for CO_2 capture. Greenh Gases: Sci Technol 3:30–39

Chen C, Park D-W, Ahn W-S (2014) CO_2 capture using zeolite 13X prepared from bentonite. Appl Surf Sci 292:63–67

Choi W, Park J, Kim C, Choi M (2021) Structural effects of amine polymers on stability and energy efficiency of adsorbents in post-combustion CO_2 capture. Chem Eng J 408:127289

Cui S, Cheng W, Shen X, Fan M, Russell AT, Wu Z, Yi X (2011) Mesoporous amine-modified SiO_2 aerogel: a potential CO_2 sorbent. Energy Environ Sci 4:2070–2074

Demilecamps A, Beauger C, Hildenbrand C, Rigacci A, Budtova T (2015) Cellulose–silica aerogels. Carbohyd Polym 122:293–300

Doan TKQ, Chiang KY (2022) Characteristics and kinetics study of spherical cellulose nanocrystal extracted from cotton cloth waste by acid hydrolysis. Sustain Environ Res 32:1–14

Gaikwad S, Kim S-J, Han S (2019) CO_2 capture using amine-functionalized bimetallic mil-101 mofs and their stability on exposure to humid air and acid gases. Microporous Mesoporous Mater 277:253–260

Gu H, Liu C, Zhu J, Gu J, Wujcik EK, Shao L, Wang N, Wei H, Scaffaro R, Zhang J (2018) Introducing advanced composites and hybrid materials. Springer, pp 1–5

Guo Y, Tan C, Wang P, Sun J, Yan J, Li W, Zhao C, Lu P (2019) Kinetic study on CO_2 adsorption behaviors of amine-modified co-firing fly ash. J Taiwan Inst Chem Eng 96:374–381

Hasan MM, Kubra KT, Hasan MN, Awual ME, Salman MS, Sheikh MC, Rehan AI, Rasee AI, Waliullah RM, Islam MS, Khandaker S, Islam A, Hossain MS, Alsukaibi AKD, Alshammari HM, Awual MR (2023) Sustainable ligand-modified based composite material for the selective and effective cadmium (II) capturing from wastewater. J Mol Liq 371:121125

Hasan MN, Salman MS, Islam A, Znad H, Hasan MM (2021a) Sustainable composite sensor material for optical cadmium (II) monitoring and capturing from wastewater. Microchem J 161:105800

Hasan MN, Shenashen M, Hasan MM, Znad H, Awual MR (2021b) Assessing of cesium removal from wastewater using functionalized wood cellulosic adsorbent. Chemosphere 270:128668

Hsan N, Dutta PK, Kumar S, Bera R, Das N (2019) Chitosan grafted graphene oxide aerogel: synthesis, characterization and carbon dioxide capture study. Int J Biol Macromol 125:300–306

Islam A, Teo SH, Taufiq-Yap YH, Ng CH, Vo D-VN, Ibrahim ML, Hasan MM, MaR K, Nur ASM, Awual MR (2021) Step towards the sustainable toxic dyes removal and recycling from aqueous solution- a comprehensive review. Resour Conserv Recycl 175:105849

Jeong-Potter C, Farrauto R (2021) Feasibility study of combining direct air capture of CO_2 and methanation at isothermal conditions with dual function materials. Appl Catal B 282:119416

Jiang F, Hu S, Hsieh Y-L (2018) Aqueous synthesis of compressible and thermally stable cellulose nanofibril–silica aerogel for CO_2 adsorption. ACS Appl Nano Mater 1:6701–6710

Jiang X, Kong Y, Zou H, Zhao Z, Zhong Y, Shen X (2021) Amine grafted cellulose aerogel for CO_2 capture. J Porous Mater 28:93–97

Kaur P, Sharma N, Munagala M, Rajkhowa R, Aallardyce B, Shastri Y, Agrawal R (2021) Nanocellulose: resources, physiochemical properties, current uses and future applications. Front Nanotech 3:747329

Keshavarz L, Ghaani MR, Macelroy JD, English NJ (2021) A comprehensive review on the application of aerogels in CO_2-adsorption: materials and characterisation. Chem Eng J 412:128604

Khedkar MV, Somvanshi SB, Humbe AV, Jadhav K (2019) Surface modified sodium silicate based superhydrophobic silica aerogels prepared via ambient pressure drying process. J Non-Cryst Solids 511:140–146

Kiliyankil VA, Fugetsu B, Sakata I, Wang Z, Endo M (2021) Aerogels from copper (II)-cellulose nanofibers and carbon nanotubes as absorbents for the elimination of toxic gases from air. J Colloid Interface Sci 582:950–960

Kong Y, Shen X, Cui S (2016a) Amine hybrid zirconia/silica composite aerogel for low-concentration co2 capture. Microporous Mesoporous Mater 236:269–276

Kong Y, Shen X, Cui S, Fan M (2015) Facile synthesis of an amine hybrid aerogel with high adsorption efficiency and regenerability for air capture via a solvothermal-assisted sol–gel process and supercritical drying. Green Chem 17:3436–3445

Kong Y, Shen X, Fan M, Yang M, Cui S (2016b) Dynamic capture of low-concentration CO_2 on amine hybrid silsesquioxane aerogel. Chem Eng J 283:1059–1068

Kubra KT, Salman MS, Hasan MN (2021) Enhanced toxic dye removal from wastewater using biodegradable polymeric natural adsorbent. J Mol Liq 328:115468

Lee S-Y, Park S-J (2015) A review on solid adsorbents for carbon dioxide capture. J Ind Eng Chem 23:1–11

Li M, Jiang H, Xu D, Yang Y (2017) A facile method to prepare cellulose whiskers–silica aerogel composites. J Sol-Gel Sci Technol 83:72–80

Li Y, Grishkewich N, Liu L, Wang C, Tam KC, Liu S, Mao Z, Sui X (2019) Construction of functional cellulose aerogels via atmospheric drying chemically cross-linked and solvent exchanged cellulose nanofibrils. Chem Eng J 366:531–538

Linneen NN, Pfeffer R, Lin Y (2014) CO_2 adsorption performance for amine grafted particulate silica aerogels. Chem Eng J 254:190–197

Liu J, Xie H, Wang Q, Chen S, Hu Z (2020) Influence of pore structure on shale gas recovery with CO_2 sequestration: insight into molecular mechanisms. Energy Fuels 34:1240–1250

Mazrouaa AM, Mansour NA, Abed MY, Youssif MA, Shenashen MA, Awual MR (2019) Nano-composite multi-wall carbon nanotubes using poly(p-phenylene terephthalamide) for enhanced electric conductivity. J Environ Chem Eng 7:103002

Miao Y, Luo H, Pudukudy M, Zhi Y, Zhao W, Shan S, Jia Q, Ni Y (2020a) CO_2 capture performance and characterization of cellulose aerogels synthesized from old corrugated containers. Carbohyd Polym 227:115380

Miao Y, Pudukudy M, Zhi Y, Miao Y, Shan S, Jia Q, Ni Y (2020b) A facile method for in situ fabrication of silica/cellulose aerogels and their application in CO_2 capture. Carbohyd Polym 236:116079

Mohd NH, Kargazadeh H, Miyamoto M, Uemiya S, Sharer N, Baharum A, Peng TL, Ahmad I, Yarmo MA, Othaman R (2021) Aminosilanes grafted nanocrystalline cellulose from oil palm empty fruit bunch aerogel for carbon dioxide capture. J Market Res 13:2287–2296

Papa E, Medri V, Paillard C, Contri B, Murri AN, Vaccari A, Landi E (2019) Geopolymer-hydrotalcite composites for CO_2 capture. J Clean Prod 237:117738

Salman MS, Hasan MN, Hasan MM, Kubra KT, Sheikh MC, Rehan AI, Waliullah RM, Rasee AI, Awual ME, Hossain MS, Alsukaibi AKD, Alshammari HM, Awual MR (2023a) Improving copper (II) ion detection and adsorption from wastewater by the ligand-functionalized composite adsorbent. J Mol Struct 1282:135259

Salman MS, Sheikh MC, Hasan MM, Hasan MN, Kubra KT, Rehan AI, Awual ME, Rasee AI, Waliullah RM, Hossain MS, Khaleque MA, Alsukaibi AKD, Alshammari HM, Awual MR (2023b) Chitosan-coated cotton fiber composite for efficient toxic dye encapsulation from aqueous media. Appl Surf Sci 622:157008

Salman MS, Znad H, Hasan MN, Hasan MM (2021) Optimization of innovative composite sensor for Pb (II) detection and capturing from water samples. Microchem J 160:105765

Sanz R, Calleja G, Arencibia A, Sanz-Pérez E (2010) CO_2 adsorption on branched polyethyleneimine-impregnated mesoporous silica SBA-15. Appl Surf Sci 256:5323–5328

Sepahvand S, Jonoobi M, Ashori A, Gauvin F, Brouwers H, Oksman K, Yu Q (2020) A promising process to modify cellulose nanofibers for carbon dioxide (CO_2) adsorption. Carbohyd Polym 230:115571

Serna-Guerrero R, Sayari A (2010) Modeling adsorption of CO_2 on amine-functionalized mesoporous silica. 2: Kinetics and breakthrough curves. Chem Eng J 161:182–190

Shi J, Lu L, Guo W, Zhang J, Cao Y (2013) Heat insulation performance, mechanics and hydrophobic modification of cellulose–SiO_2 composite aerogels. Carbohyd Polym 98:282–289

Song G, Zhu X, Chen R, Liao Q, Ding Y-D, Chen L (2016) An investigation of CO_2 adsorption kinetics on porous magnesium oxide. Chem Eng J 283:175–183

Sun J, Shang M, Zhang M, Yu S, Yuan Z, Yi X, Filatov S, Zhang J (2022) Konjac glucomannan/cellulose nanofibers composite aerogel supported HKUST-1 for CO_2 adsorption. Carbohyd Polym 293:119720

Tang L, Zhuang S, Hong B, Cai Z, Chen Y, Huang B (2019) Synthesis of light weight, high strength biomass-derived composite aerogels with low thermal conductivities. Cellulose 26:8699–8712

Wang C, Okubayashi S (2019) Polyethyleneimine-crosslinked cellulose aerogel for combustion CO_2 capture. Carbohyd Polym 225:115248

Wang X, He C, He H, Xie W (2022) Simulation and experimental research on nonlinear ultrasonic testing of composite material porosity. Appl Acoust 188:108528

Wickramaratne NP, Jaroniec M (2013) Activated carbon spheres for CO_2 adsorption. ACS Appl Mater Interfaces 5:1849–1855

Wörmeyer K, Smirnova I (2013) Adsorption of CO_2, moisture and ethanol at low partial pressure using aminofunctionalised silica aerogels. Chem Eng J 225:350–357

Yang F, Zhu X, Wu J, Wang R, Ge T (2022) Kinetics and mechanism analysis of CO_2 adsorption on lix@ zif-8 with core shell structure. Powder Technol 399:117090

Yoro KO, Amosa MK, Sekoai PT, Mulopo J, Daramola MO (2020) Diffusion mechanism and effect of mass transfer limitation during the adsorption of CO_2 by polyaspartamide in a packed-bed unit. Int J Sustain Eng 13:54–67

Yu F, Wu Y, Zhang W, Cai T, Xu Y, Chen X (2016) A novel aerogel sodium-based sorbent for low temperature CO_2 capture. Greenh Gases: Sci Technol 6:561–573

Zhang T, Zhang W, Zhang Y, Shen M, Zhang J (2020) Gas phase synthesis of aminated nanocellulose aerogel for carbon dioxide adsorption. Cellulose 27:2953–2958

Zheng Q, Cai Z, Gong S (2014) Green synthesis of polyvinyl alcohol (PVA)–cellulose nanofibril (CNF) hybrid aerogels and their use as superabsorbents. J Mater Chem A 2:3110–3118

Zhou G, Wang K, Liu R, Tian Y, Kong B, Qi G (2021) Synthesis and CO_2 adsorption performance of tepa-loaded cellulose whisker/silica composite aerogel. Colloids Surf, A 631:127675

Zhou L, Zhai Y-M, Yang M-B, Yang W (2019) Flexible and tough cellulose nanocrystal/polycaprolactone hybrid aerogel based on the strategy of macromolecule cross-linking via click chemistry. ACS Sustain Chem Eng 7:15617–15627